Check for updates

JGR Planets

RESEARCH ARTICLE
10.1029/2022JE007730

Extensive Lunar Surface Disturbance at the Chang'e-5 Mission Landing Site: Implications for Future Lunar Base Design and Construction

Le Qiao[1,2], Marcel Hess[3], Luyuan Xu[2,4], Christian Wöhler[3], James W. Head[5], Jian Chen[1], Yiran Wang[6], Roberto Bugiolacchi[2,4], Ayang Xiao[1], Feng Zhang[7], and Zongcheng Ling[1]

[1]Shandong Key Laboratory of Optical Astronomy and Solar-Terrestrial Environment, School of Space Science and Physics, Institute of Space Sciences, Shandong University, Weihai, China, [2]State Key Laboratory of Lunar and Planetary Sciences, Macau University of Science and Technology, Macau, China, [3]Image Analysis Group, TU Dortmund University, Dortmund, Germany, [4]Macau Center for Space Exploration and Science, CNSA, Macau, China, [5]Department of Earth, Environmental and Planetary Sciences, Brown University, Providence, RI, USA, [6]Department of Earth and Space Sciences, Southern University of Science and Technology, Shenzhen, China, [7]State Key Laboratory of Space Weather, National Space Science Center, Chinese Academy of Sciences, Beijing, China

Abstract Lunar surface disturbances by spacecraft engine jets are of particular concern in the current new phase of lunar exploration, when dozens of landing missions and permanent bases are being planned. Some of these exploration efforts will involve multiple landings and liftoffs around the same lunar site; thus, it is essential to evaluate their effect on astronauts and assets on the lunar surface. Here, we assess the surface disturbances during the Chang'e-5 landing and liftoff procedures through the photometric analysis of high-resolution multi-temporal surface and orbital images. Centimeter-scale surface images reveal a four-stage evolution of the landing plume impingement over a period of ~50 s, which involves phenomena such as dust devils and streaks, and displacement of cobbles. Temporal-ratio calculation of orbital images (including one acquired between landing and liftoff) enables the first direct observation of ascent plume effects. The ascent blast zone consists of two separated sub-areas (~3,400 m^2 in total), which is nearly twice larger than that of the landing blast zone. The final disturbed surface is characterized by a central main zone (~2,300 m^2) surrounded by a marginal diffuse zone (~15,300 m^2). Phase-ratio analyses suggest that plume impingement destroys the micro-porous structure of the uppermost regolith. We estimate that future lunar landers (e.g., SpaceX's Starship) may cause significant lunar surface disturbances over an area of square kilometers. Our results provide unique insights into Chang'e-5 mission activities, and instructive references for the planning of future lunar endeavors, including the design and construction of surface experiment packages and permanent lunar bases.

Plain Language Summary When spacecraft land on or liftoff from the lunar surface, the release of huge volumes of gases from retrorocket engines significantly disturbs the lunar surface beneath it. These surface disturbance effects are of particular concern as several landing missions and permanent lunar bases are being planned. It is necessary to evaluate how people and instruments will be affected by these disturbances. Here, we study the surface modifications at the Chang'e-5 mission landing site using high-resolution surface and orbital images. Centimeter-scale Chang'e-5 images reveal dramatic surface phenomena during the landing procedure over a period of ~50 s, including dust devils and movements of cobbles. Orbital images obtained at different times enable the first direct observation of surface disturbances during liftoff, which are unexpectedly about twice more extensive than those during landing. The final disturbed surface is composed of a central main zone and a marginal diffuse zone. We predict that future lunar landers (e.g., SpaceX's Starship) may disturb the lunar surface over an area of several square kilometers. Our results provide unique insights into an understudied aspect of the Chang'e-5's mission, and important references for future lunar explorations, including the design and emplacement of lunar surface instruments and permanent lunar bases.

Key Points:

- High-resolution multi-temporal surface and orbital images reveal extensive surface disturbance at the Chang'e-5 landing site
- Lunar surface disturbed during liftoff is nearly twice larger than that during landing, much more extensive than previously assumed
- This provides a unique insight into Chang'e-5 mission activities and instructive references for future lunar base design and construction

Supporting Information:

Supporting Information may be found in the online version of this article.

Correspondence to:

L. Qiao,
leqiao.geo@gmail.com

Citation:

Qiao, L., Hess, M., Xu, L., Wöhler, C., Head, J. W., Chen, J., et al. (2023). Extensive lunar surface disturbance at the Chang'e-5 mission landing site: Implications for future lunar base design and construction. *Journal of Geophysical Research: Planets*, *128*, e2022JE007730. https://doi.org/10.1029/2022JE007730

Received 6 JAN 2023
Accepted 13 JUN 2023
Corrected 4 JUL 2023

This article was corrected on 4 JUL 2023. See the end of the full text for details.

1. Introduction

A new era of lunar exploration, following the Apollo/Luna period in the middle of the last century, is emerging. During the past decade, over a dozen spacecraft have orbited, landed on, and roved across the Moon. In the coming years, this trend will increase through the efforts of multiple organizations, including both emerging spacefaring nations and commercial entities. For instance, nearly 10 spacecraft are planned to fly to the

© 2023. American Geophysical Union. All Rights Reserved.

Moon in the single year of 2023 (Pickrell, 2022; https://www.technologyreview.com/2020/02/27/905641/lunar-missions-before-nasa-2024-artemis-moon-landing-space-x-mining).

Among the forthcoming armada of spacecraft heading to the Moon, several are designed to land on its surface. Compared to orbital missions designed for remote sensing investigations, in situ data collection can offer infinitely higher spatial resolution and direct access to the selected targets' properties. However, high-frequency landing activities can cause surface modifications corrupting the pristine status of its components. Any powered lunar landing attempt will inevitably release a considerable amount of exhaust gases (typically on the scale of tons; e.g., Watkins et al., 2020), which could significantly disturb the landing area surface and contaminate the extremely tenuous lunar atmosphere (e.g., Clegg et al., 2014; Prem et al., 2020). Such exhaust plume impingement effects by retrorockets were best witnessed by the Apollo 12 mission, which landed only 155 m from the earlier Surveyor III lander. The Apollo 12 astronauts approached Surveyor III and returned pieces of the Surveyor III craft to Earth. Laboratory analysis showed that the Surveyor III hardware was significantly scoured and pitted by the Apollo 12 exhaust ejecta with velocities up to 2 km/s (Brownlee et al., 1972; Immer, Metzger et al., 2011). These effects are of particular concern in the contemporary new wave of lunar exploration, when many space agencies are going forward to the Moon to stay, for instance, the International Lunar Research Station proposed jointly by China and Russia (CNSA & Roscosmos, 2021), and the Artemis Base Camp by the United States (NASA, 2020). During the construction of these permanent lunar outposts, numerous missions may land at and ascend from the same site. It is paramount to evaluate how the astronauts, collected samples, scientific instruments, and other assets on the lunar surface will be affected by the plume impingements during these landing and ascending activities.

In December 2020, China's Chang'e-5 mission successfully landed in and returned lunar samples from a basaltic mare area on the western nearside of the Moon (Li et al., 2022; Qian, Xiao, Head, van der Bogert et al., 2021; Qian, Xiao, Wang, et al., 2021; Qiao, Chen et al., 2021; Zhou et al., 2022), the first robotic lunar sample return mission since the Soviet Luna 24 in 1976. The entire landing process and disturbances of the landing area surface were continuously recorded by the cameras onboard the Chang'e-5 lander (Zhou et al., 2022). In addition, the landing area of the Chang'e-5 craft has also been frequently imaged by the high-resolution cameras onboard NASA's Lunar Reconnaissance Orbiter (LRO; Robinson et al., 2010), both before and after the Chang'e-5 landing (at a frequency of no less than one image per month after the landing; Table S1 in Supporting Information S1). In particular, the LRO flew over and imaged the Chang'e-5 landing site the day following its touchdown while Chang'e-5 was collecting samples on the lunar surface (https://www.lroc.asu.edu/posts/1172). These sophisticated high-resolution surface and orbital imaging observations provide an unprecedented opportunity for evaluating the surface disturbance effects of the Chang'e-5 landing and ascending activities.

In this work, we employ high-resolution multi-temporal Chang'e-5 surface images and LRO orbital images to assess the surface disturbance effects of descent, landing and ascent procedures during the Chang'e-5 mission. Our analyses provide a unique insight into Chang'e-5 mission activities and informative references for the planning of future lunar landing exploration, including the design and construction of lunar surface experiment packages and permanent lunar bases.

2. Data and Methodology

2.1. Chang'e-5 Surface Image Data Analysis

We use image data acquired by the Landing Camera (LCAM) during the descent routine and the Panoramic Camera (PCAM) after the lunar landing, both onboard the Chang'e-5 lander (Zhou et al., 2022), to document surface disturbances by the landing engine exhaust plumes. The LCAM is one of the four scientific instruments onboard the Chang'e-5 spacecraft. It was designed to acquire optical images of the lunar surface beneath the Chang'e-5 lander. It operates in two modes, both with an acquisition rate of one image per second. In mode 1, it has a field of view (FOV) of 59° × 45° over the image size of 2,352 × 1,728 pixels, while in mode 2, the FOV is 27.5° × 27.5° and the image size is 1,024 × 1,024 pixels. The LCAM typically worked in a routine with 5 s in mode 1 followed by 1 s in mode 2 (Zhou et al., 2022). Level 2A LCAM image data are provided by the Ground Research and Application System (GRAS) of China's Lunar and Planetary Exploration Program and can be directly used for morphological analysis. The PCAM is a pair of color stereo cameras mounted on the rotating mechanism of the Chang'e-5 lander. They are designed to acquire images for the sample collection process and

the lunar surface surrounding the lander, with an image size of 2,352 × 1,728 pixels (Zhou et al., 2022). A mosaic of PCAM images was produced and released by the GRAS, which is used in this study.

2.2. Orbital Image and Altimetry Data Processing and Analysis

We analyzed the morphology, topography, and geological context of the Chang'e-5 landing area using the latest high-resolution orbital image and altimetry data sets from the LRO Narrow-Angle Camera (LROC NAC), the Kaguya Terrain Camera (TC), the LROC NAC photogrammetry digital terrain model (DTM) and the blended SELENE (Kaguya) TC DTM/LRO Lunar Orbiter Laser Altimeter (LOLA) topography (SLDEM2015). The NAC is a pair of monochrome push-broom cameras onboard NASA's LRO spacecraft, designed to image the lunar surface with a ground resolution of ∼0.5 m/pixel (from the nominal 50 km orbit; Robinson et al., 2010). The LROC NAC images were processed, calibrated, and map-projected to a common resolution of 1.6 m/pixel using the USGS Integrated Software for Imagers and Spectrometers (ISIS3, Anderson et al., 2004). The LROC NAC DTM topography was generated from two stereo NAC observations and has a 3 m horizontal sampling size and better than 3 m relative vertical precision (Henriksen et al., 2017). The TC is a high-resolution panchromatic stereo camera onboard Japan's SELENE (Kaguya) lunar orbiter, which mapped the entire lunar surface with a pixel size of 10 m from a nominal altitude of 100 km (Haruyama et al., 2008). The SLDEM2015 is a topography product of the lunar surface (Barker et al., 2016) created from LRO LOLA laser altimetric data points (Smith et al., 2010) and Kaguya TC photogrammetry DTM (Haruyama et al., 2012). It has a spatial resolution of 512 pixels/degree (∼43 m at the landing site) and vertical altimetric accuracy of ∼3–4 m. Processed and geo-referenced data products are available for the NAC DTM, TC image and SLDEM2015 topography data sets, and can be used directly for morphological and topographical analyses.

In addition, ratio images calculated from two different NAC frames are used to study the spatial extent and photometric characteristics of the blast zones produced by the Chang'e-5 craft. Suitable pairs of NAC images covering the Chang'e-5 landing site were selected for the co-registration process (Table S1 in Supporting Information S1). In the temporal ratio image calculation, NAC frames with similar illumination geometries (incidence (i), emission (e), phase (g), and subsolar azimuth (α) angles) acquired at different times (before, during, and after the Chang'e-5 mission) were used. The differences of i, e, g, and α are ∼8–11°, ∼11°, ∼1°, and ∼11–21°, respectively, for the during/before and after/during temporal-ratio image pairs. The after/before image pair has very close illumination geometries: the differences of i, e, and g are all less than 1°, and the difference of α is ∼5°. In the phase-ratio image calculation, NAC frames with similar incidence and subsolar azimuth angles acquired following the liftoff of the Chang'e-5 ascender were selected (the differences of i and α are ∼16° and ∼114°, respectively). Similar or close illumination geometries would facilitate the alignment processing of image pairs, though this was not always possible and considerable geometrical variations still exist between the selected image pairs (Table S1 in Supporting Information S1). These geometrical differences may introduce reflectance disparity between images for undisturbed lunar surface, while the relative reflectance variations observed in the same frame or ratio image are still useful for surface change analysis. For post-mission phase-ratio analysis, we placed the NAC image with a larger phase angle in the numerator and the smaller phase angle image in the denominator; consequently, smaller phase-ratio values indicate gentler phase curve slopes and vice versa. The selected NAC images were manually co-registered to one reference image (M1114519536LE) using an in-house MATLAB routine by marking a set of pairs of corresponding points based on small craters and estimating the best-fit projective transformation between the image under study and the reference image.

3. Results

3.1. The Chang'e-5 Mission and Its Landing Site

The Chang'e-5 touched down on the lunar surface at 15:11 UTC, on 1 December 2020. After spending two Earth days on the lunar surface gathering ∼1.7 kg samples, the ascent stage blasted off from the landing site on 3 December 2020 at 15:10. The dry mass of the lander and ascender combination is about 1.2 tons (Hong et al., 2022; Shu et al., 2021). The lander was powered by the main engine with a maximum of 7,500 N of thrust, and the ascent vehicle was equipped with a main 3,000 N thrust engine. Both propulsion systems use dinitrogen tetroxide (N_2O_4) and monomethyl hydrazine (CH_3NHNH_2) as rocket propellants. During the powered descent procedure, ∼1.9 tons of propellant was consumed and ∼0.39 tons was burned to lift the ascender into lunar orbit (Hong

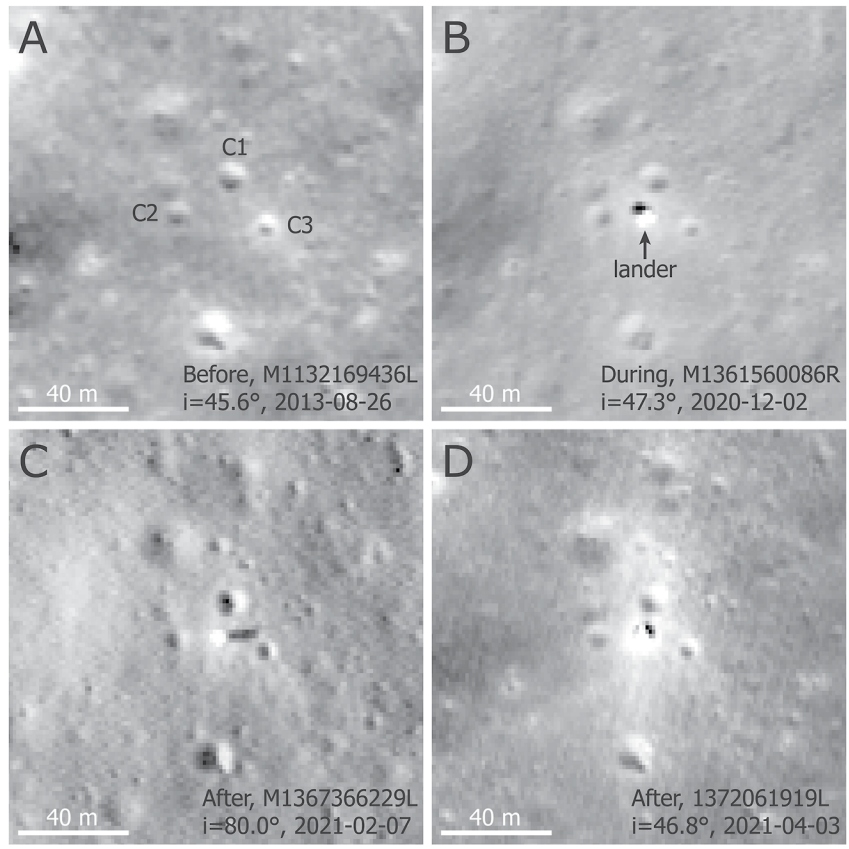


Figure 1. The Chang'e-5 lander and the adjacent lunar surface. LROC Narrow-Angle Camera images of the landing area (200 × 200 m extent) taken (a) before, (b) during, and (c), (d) after the mission. The lander is indicated by the arrow and the three small craters (C1-C3) surrounding the lander are labeled. The image IDs, solar incidence angle (i) and acquisition dates are displayed on each panel. All maps in this paper are projected into a Mollweide equal-area projection, with a central meridian of 51.8°W, and north is toward the top, unless otherwise specified.

et al., 2022). On the basis of the chemical reaction equation ($5N_2O_4 + 4N_2H_3CH_3 \rightarrow 4CO_2 + 12H_2O + 9N_2$) calculation, up to 0.77 tons of water (H_2O), 0.90 tons of nitrogen (N_2), and 0.63 tons of carbon dioxide (CO_2) are estimated to have been released during the descent and ascent procedures.

Soon after the landing of the Chang'e-5 craft, LRO passed over the landing site at an altitude of 115 km and made an oblique (13° off-nadir slew) imaging observation of the lander (Figure 1b). Compared with an LROC NAC image (Figure 1a) acquired years before the Chang'e-5 landing, the Chang'e-5 lander is clearly seen as a bright spot. In addition, a circular diffuse region with elevated brightness (referred to as a "blast zone") is also observed to surround the lander. In another NAC image with similar solar incidence angles obtained months after the ascent vehicle lifted off (Figure 1d), the blast zone appears to be expanded and has become elongated, indicating considerable plume impingement effects caused by the ascent engine jets. This is the first-ever orbital observation of plume effects during lunar surface ascending activities, as previous investigations only have pre-mission and/or post-mission images, but lack such "during-mission" images (between lunar landing and surface ascending) (Clegg et al., 2014; Clegg-Watkins et al., 2016; Kaydash et al., 2011). In an additional post-mission image (Figure 1c) taken at low solar elevation (∼10°), the remaining lander casts a long shadow to the east, indicating the very steep topographic relief across the lander, making it stand out against nearby small fresh craters.

Meter-scale NAC images and the derived topography data reveal that the localized landing area is relatively flat and monotonous, dominated by small impact craters superposed on basaltic mare plains (Figures 1 and 2). The lander is centered within a triangle of sub-decameter craters (informally termed C1-C3 craters). Very-high-resolution (centimeter pixel size) images acquired during the powered descent procedure by the Chang'e-5 LCAM (Table S2 in Supporting Information S1) show that these three craters are morphologically degraded with shallow depths

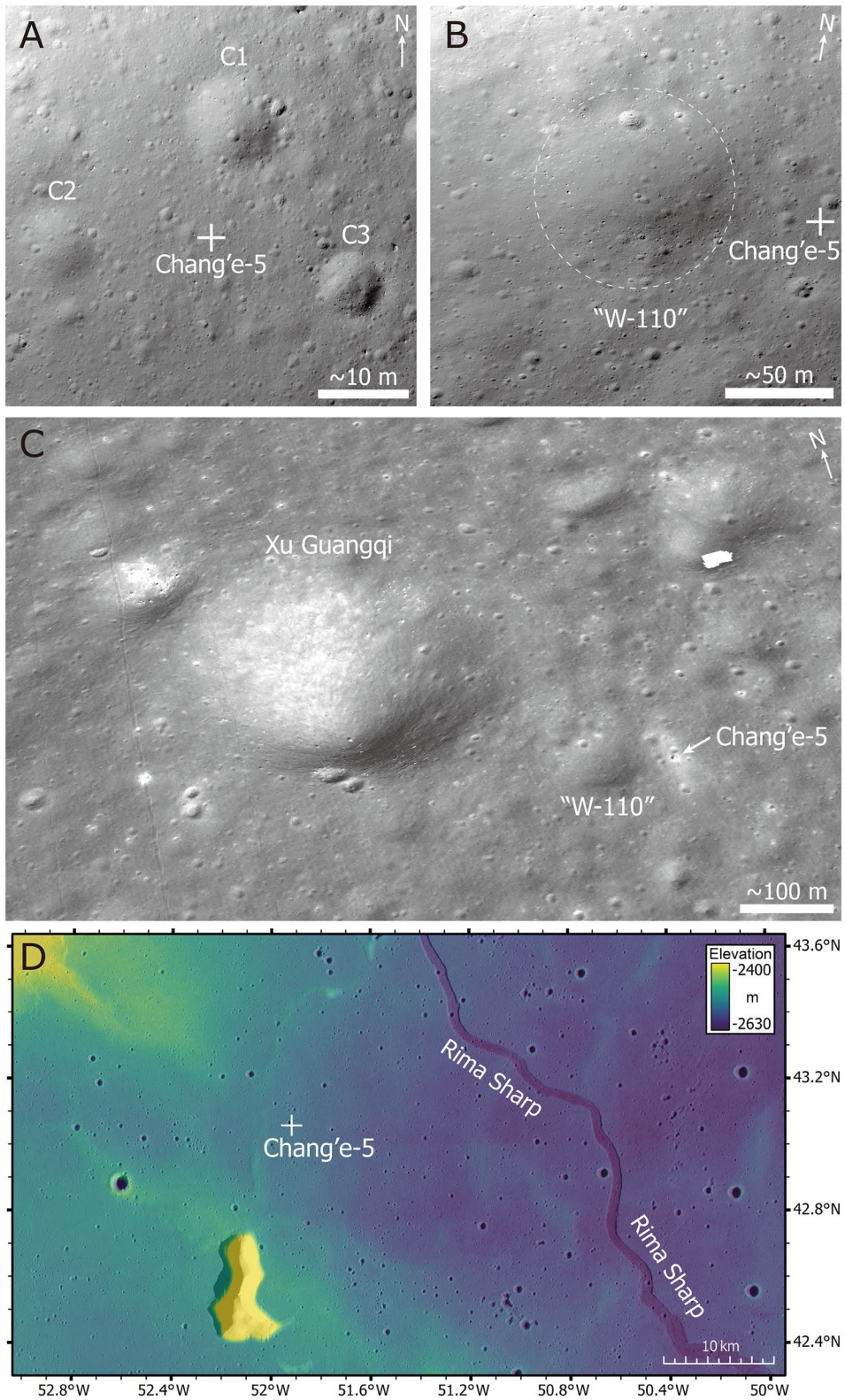

A
N
C1
C2
C3
Chang'e-5
~10 m
B
N
Chang'e-5
"W-110"
~50 m
C
N
Xu Guangqi
Chang'e-5
"W-110"
~100 m
D
Elevation
-2400
m
-2630
Rima Sharp
Rima Sharp
Chang'e-5
10 km
43.6°N
43.2°N
42.8°N
42.4°N
52.8°W
52.4°W
52°W
51.6°W
51.2°W
50.8°W
50.4°W
50°W

Figure 2.

and subtle rim crests, though the C3 crater is comparatively fresher than the other two, with some tiny boulders scattered in the crater interior (Figure 2a). In addition, another conspicuous crater (informally designated as the "W-110" crater) lies in close proximity west of the Chang'e-5 lander (Figure 2b). The diameter of this crater is ~110 m and the Chang'e-5 lander is ~86 m away from the crater center. Based on the classic ejecta distribution model (Melosh, 1989), the Chang'e-5 spacecraft would have landed over the continuous ejecta blanket of the W-110 crater. Moreover, the Xu Guangqi crater, ~400 m in diameter, which is located ~220 m northwest of the Chang'e-5 lander (Figure 2c), should have also ejected many materials into the direction of the landing site, probably buried below the ejecta blanket of the W-110 crater. Previous studies have demonstrated that topographical depressions, for instance, the Surveyor crater at the Apollo 12 landing area, act as effective containers for rocket exhausts (Clegg et al., 2014); we aim to assess how the Chang'e-5 rocket plumes would have interacted with these nearby craters.

Regionally, the Chang'e-5 landing area is located at the central portion of a very extensive basaltic mare unit in the western nearside of the Moon (Figure 2d). This mare unit spreads across ~35,000 km^2 and is among the youngest lunar maria (Hiesinger et al., 2011; Qian, Xiao, Head, van der Bogert et al., 2021; Qiao, Xu et al., 2021). The most prominent geological feature in the Chang'e-5 mare unit is the sinuous rille Rima Sharp which lies ~17 km east of the landing site (Figure 2d). This rille has been measured to be over 500 km long and is regarded as the longest sinuous rille on the Moon (Hurwitz et al., 2013). More recent work suggests that Rima Sharp is actually formed from two rilles emanating from different sources and meeting in the middle (Qian, Xiao, Head, & Wilson, 2021). Sinuous rilles are generally interpreted to be formed by very high-volume and long-lasting volcanic eruptions on the Moon (Head & Wilson, 2017), indicating that Rima Sharp probably carried the lava that produced the extensive mare unit surrounding the Chang'e-5 landing site (Xu & Qiao, 2022).

3.2. Surface Disturbances by Rocket Plumes as Seen From the Lunar Surface

The release of tons of rocket exhaust gases during the Chang'e-5 powered descent procedure was predicted to interact vigorously with the landing area surface and introduce significant surface erosion. These plume impingement processes can be analyzed in detail from centimeter-scale surface images acquired by the Chang'e-5 LCAM during the descent sequence and by the PCAM following touchdown (Table S2 in Supporting Information S1). The LCAM started to image the landing area surface about 8 min (~500 s) before the surface touchdown. The imaging sequence worked at a frequency of one frame per second, with five frames in mode 1 (LCAM-1; 2,352 × 1,728 pixels) followed by one frame in mode 2 (LCAM-2; 1,024 × 1,024 pixels). Images acquired in each mode are numbered individually, both from 0001, though only mode 1 images are used in this work. The sequences of Chang'e-5 surface images reveal a four-stage evolution for the interactions between the rocket exhaust gases and lunar surface materials.

The plume impingement effects were initiated when the descent vehicle approached the lunar surface at an altitude of about 14 m. Retrorocket exhausts hit the surface, which caused the lifting of lunar regolith and dust particles. A thin sheet of these particles increases light scattering, resulting in the growth of haze and the decline of visual contrast (cf. Figures 3a and 3b). Similar phenomena have been reported and investigated by the Apollo astronauts during the landing processes (Gold, 1970; Metzger et al., 2011; NASA Manned Space Center, 1969, 1972). A crescent dust devil is observed during this "haze growth" phase, interpreted as the impingement point below the lander vehicle nozzle and the source of the dust sheet. The local area in the proximity of the impingement point appears darker than the surroundings, which is attributed to its highly pitted textures caused by the powerful exhaust plumes (Hapke, 1972).

As the lander vehicle descended further, the shock wave of the plume was compressed, increasing the plume shear stress (Roberts, 1963). The initially rarefied haze became progressively thicker and was finally shaped into apparent streaks by the increasing gas density and velocity (Figures 3c and 3d). These ray-like jets (streaks) are observed to emanate radially from the impingement point and are often obstructed by relatively large boulders sitting on the surface. The streaks became increasingly more abundant and well-outlined as the lander approached

Figure 2. The geological context of the Chang'e-5 landing site at various scales. (a) The three sub-decameter craters surrounding the lander, Chang'e-5 LCAM frame 0396 (see full data ID in Table S2 of the Supporting Information S1), (b) the "W-110" crater west of the lander, LCAM frame 0347 (Table S2 in Supporting Information S1), (c) 3-D perspective view of the western vicinity of the lander, including the Xu Guangqi and "W-110" craters, LROC Narrow-Angle Camera (NAC) M1374421274L image overlain on LROC NAC DTM topography, 2.0 vertical exaggeration, and (d) 70 × 30 km area surrounding the landing site, blended SELENE (Kaguya) TC DTM/LRO Lunar Orbiter Laser Altimeter (LOLA) (SLDEM2015) topography overlain on Kaguya Terrain Camera (TC) map with morning illumination.

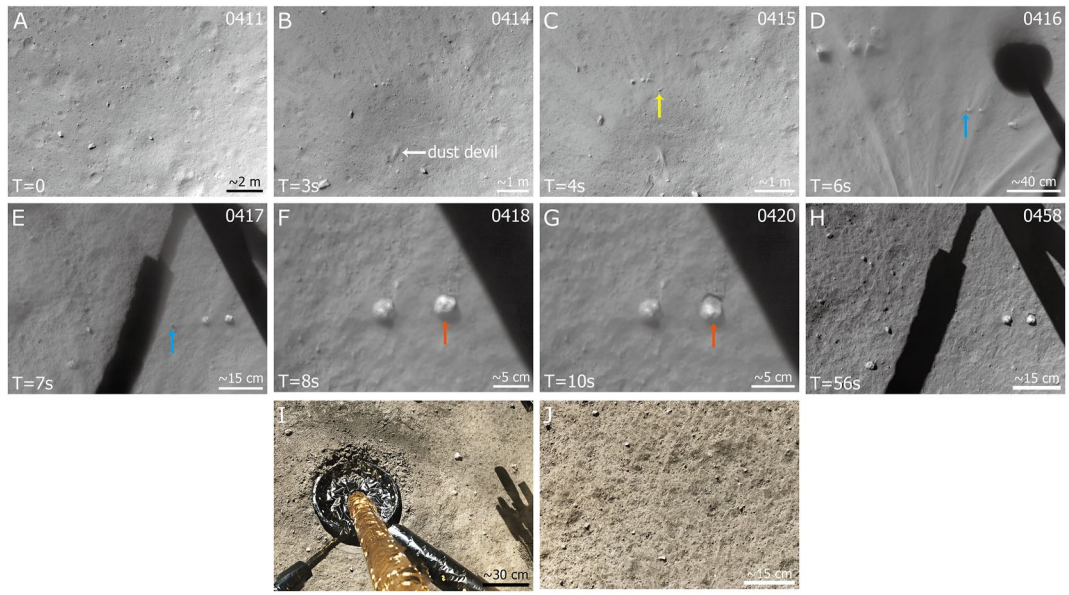


Figure 3. Rocket exhaust-induced surface disturbances during the Chang'e-5 landing procedure. (a) The landing area surface before the plume impingement effects, (b) the haze growth phase, (c)–(e) the streak development phase, (f), (g) the surface erosion phase, and (h)–(j) the final resultant landscapes surrounding the lander. A dust devil, interpreted as the impingement point below the engine nozzle, is highlighted by the white arrow in panel (b). Arrows of other colors point to small gravels that have been blown away (yellow and turquoise ones) or disturbed by the plume flows (orange arrow). Panels (a–h) are Chang'e-5 Landing Camera (LCAM) mode 1 images and their abbreviated frame IDs (see full IDs in Table S2 of the Supporting Information S1) and relative acquisition time in seconds (with $T = 0$ for panel a) are labeled in each panel. Panels i and j are portions of the Panoramic Camera (PCAM) mosaic released by the Ground Research and Application System of China's Lunar and Planetary Exploration Program. In all LCAM images, the north is toward the right and the east is toward the top. In both PCAM images, the north is toward the bottom and the east is toward the right.

touchdown. Toward the end of this "streak development" phase, gravel and cobbles of a wide range of sizes were transported by the powerful plume flows (cf. Figures 3d and 3e). In one outstanding case (cf. Figures 3c and 3d), a relatively large cobble (yellow arrow in Figure 3c), with an estimated diameter of ~5 cm, was blown away to a distance of over 0.5 m (estimated from the upper edge of Figure 3d), a strong example of powerful plume effects.

About 1–2 s (from LCAM frame 0416 to 0418) before the surface touchdown, the main thrust engine shut off and the exhaust gas release rapidly turned stagnant. The engine nozzle approached the closest to the lunar surface and compressed the residual plume. Compared to the earlier stage, the plume phenomena of this phase are much less dramatic. Streaks of dust are still observable (e.g., Figures 3f and 3g) but dissipated gradually over a period of ~7 s (from LCAM frame 0416 to 0422). Numerous lunar regolith particles were mobilized by the residual plume rapidly, forming a haze-like sheet with heterogeneous reflectivity (Figures 3f and 3g). In addition, one small cobble, estimated to be ~4 cm in diameter, was shaken by the plume (cf. Figures 3f and 3g). This observed movement and removal of a large amount of surface regolith and gravel cause significant surface erosion. The lander's footpads impacted the lunar surface at the moment of touchdown and mechanically deformed and disturbed the regolith below (Figure 3i).

Finally, the residual haze dissipated completely over a period of ~40 s (until LCAM frame 0458) and the view of the landing area cleared up (Figure 3h). The final resultant landscape around the landed spacecraft appears populated by erosional remnants characterized by a wide range of pitted, hummocky, and wavy textures (Figures 3h and 3j).

3.3. Orbital Observations of Rocket Plume-Induced Surface Disturbances

Given the continual orbital observations of the Moon over the past decade, in particular, by NASA's LRO launched in 2009, lunar surface modifications caused by recently landed missions can also be investigated from orbit, for example, China's Chang'e-3 (Clegg-Watkins et al., 2016), Chang'e-4 (Gou et al., 2020), Israel's Beresheet

(http://lroc.sese.asu.edu/posts/1101), and India's Chandrayaan-2 lander (http://lroc.sese.asu.edu/posts/1131). Due to the nature of the orbit of the LRO spacecraft, its NAC camera was able to observe the Chang'e-5 landing area at high spatial resolution about once a month following touchdown (Table S1 in Supporting Information S1), thus enabling detailed analyses of the exhaust plume effects caused by the Chang'e-5 landing. In addition, the LROC NAC also imaged the landed Chang'e-5 spacecraft on the lunar surface before the ascent module's lift-off (Figure 1d), which makes it possible for the first time to evaluate the plume effects of lunar surface ascending activity independently.

We first compute the ratio of two NAC images acquired before and during (between lunar landing and surface lift-off) the Chang'e-5 mission at similar illumination/observation conditions (Figure 4a and Table S1 in Supporting Information S1). Such a temporal-ratio image directly demonstrates surface changes on terrestrial bodies. On the Moon, this technique has been employed to characterize surface changes induced by new meteoritic impacts (Kaydash et al., 2018; Robinson et al., 2015; Speyerer et al., 2016) and astronautical activities (hard and soft landings; Clegg-Watkins et al., 2016; http://lroc.sese.asu.edu/posts/1101; http://lroc.sese.asu.edu/posts/1131). In this during/before temporal-ratio image, the background maria outside the landing area has ratio values generally greater than 1 (average value of 1.3), indicating that for the "during" image more light was received at the camera sensor compared to the "before" image. As the distal background maria are not predicted to be altered by the exhaust plumes, we attribute such observed reflectivity changes to the variations in imaging geometry between the two NAC images (Table S1 in Supporting Information S1): the numerator image (during) image has smaller incidence angles than the denominator (before) image, thus relatively fewer shadows are predicted to be produced in the numerator image, leading to the higher reflectance for the unaltered surface. We calibrate this temporal-ratio image to the background maria value (Figure 4a) and find that the Chang'e-5 lander and its vicinity clearly appear as bright anomalies. The Chang'e-5 lander, as pointed out in Figure 4a, is significantly brighter than the same site before the landing, with calibrated temporal-ratio values greater than 2. Several pixels northwest of the lander have abnormally small ratio values, which is attributed to the shadows cast by the Chang'e-5 lander. The temporal ratio value generally decreases with distance from the landing site, and a small area with recognizable boundaries can be defined as the descent blast zone (outlined in Figure 4a). This zone is nearly circular in outline and measured ~52 × 43 m in size and 1,631 m^2 in surface area. The average calibrated temporal-ratio value of this blast zone is 1.11 ($1\sigma = 0.19$). In addition, a diffuse ring with a width of ~10 m appears to surround the blast zone. Temporal ratio values of this diffuse ring are slightly greater than the undisturbed background mare and decrease to the background level gradually.

Then, we construct another temporal ratio image calculated from two NAC frames obtained during and after (after surface liftoff) the Chang'e-5 mission, also under similar observation conditions (Figure 4b and Table S1 in Supporting Information S1), to assess the plume impingement effects during the ascent period. In this after/during temporal ratio image, the undisturbed background maria have relatively homogeneous ratio values, with an average value of 0.87 ($1\sigma = 0.03$). Similar to the case of the during/before image above, we suggest that the reflectance difference between the two NAC images was again due to variations in the observation geometry and smaller incidence angle for the denominator (during) image (Table S1 in Supporting Information S1). This after/during ratio image is then calibrated to the background maria (Figure 4b), which reveals that the surface alteration patterns in the vicinity of the lander appear distinct from those caused by the landing procedure (Figure 4a). The lander became notably darker in the image after the ascender lifted off, while the lander's shadow in the northwest became much brighter after the ascent. This different pattern of reflectance between the lander and its shadow is contrary to those seen in the during/before temporal ratio image above (Figure 4a). We propose that such a difference does not necessarily indicate considerable surface modifications on the lander and the shadowed regions during the ascending activity, but could again be accounted for by the variation of imaging geometries among the image pairs (Table S1 in Supporting Information S1). In the during/before temporal ratio case, the numerator image (during) has smaller incidence and phase angles than the denominator image (before), while the opposite condition applies for the after/during case. Alternatively, parts of the lander might become darker due to being burnt by the rocket jets during the ascend procedure. The lunar surface in the nearest (5–10 m distance) vicinity of the lander does not appear to be anomalous in the after/during ratio image (Figure 4b). Intriguingly, two additional small blast zones are observed to be produced during ascent. The northern one is relatively larger, with a surface area of 2,442 m^2. It is elongated in the north-south direction and measures ~73 × 56 m in dimension. The southern blast zone is relatively smaller and 920 m^2 in surface area. It is roughly circular in outline and measures ~45 × 38 m in dimension. The two blast zones have an average calibrated after/during temporal ratio

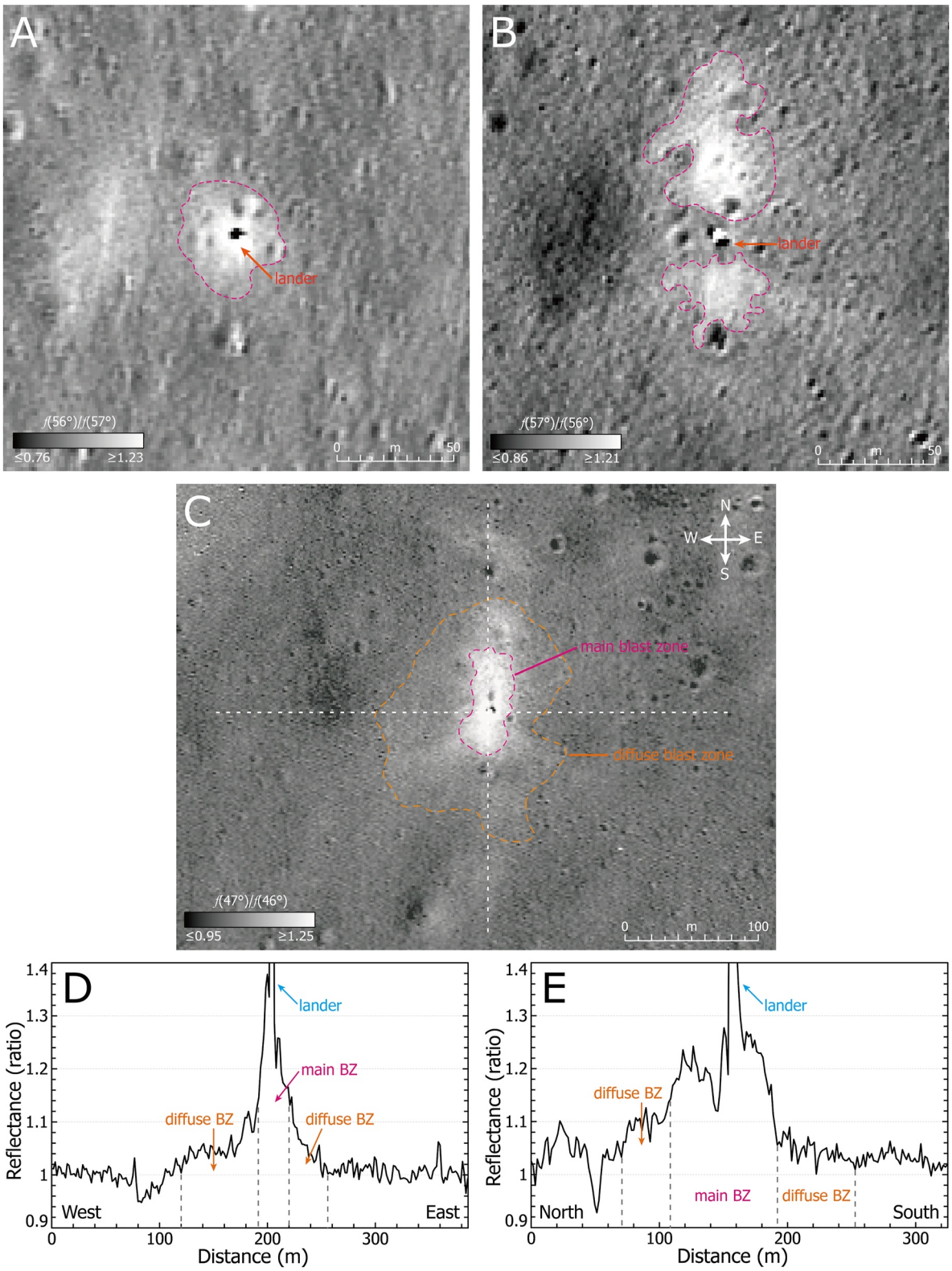


Figure 4. LROC Narrow-Angle Camera (NAC) temporal phase-ratio images and profiles for the Chang'e-5 landing area. (a) During/before (calibrated to the background maria), (b) after/during (calibrated to the background maria), and (c) after/before images, and (d) west-east and (e) north-south profiles derived from the after/before ratio image. The BZ are delineated by dashed polygons and the locations of profiles are shown as dashed lines in panel (c). The IDs of source NAC images for temporal-ratio calculations are listed in Table S1 of the Supporting Information S1.

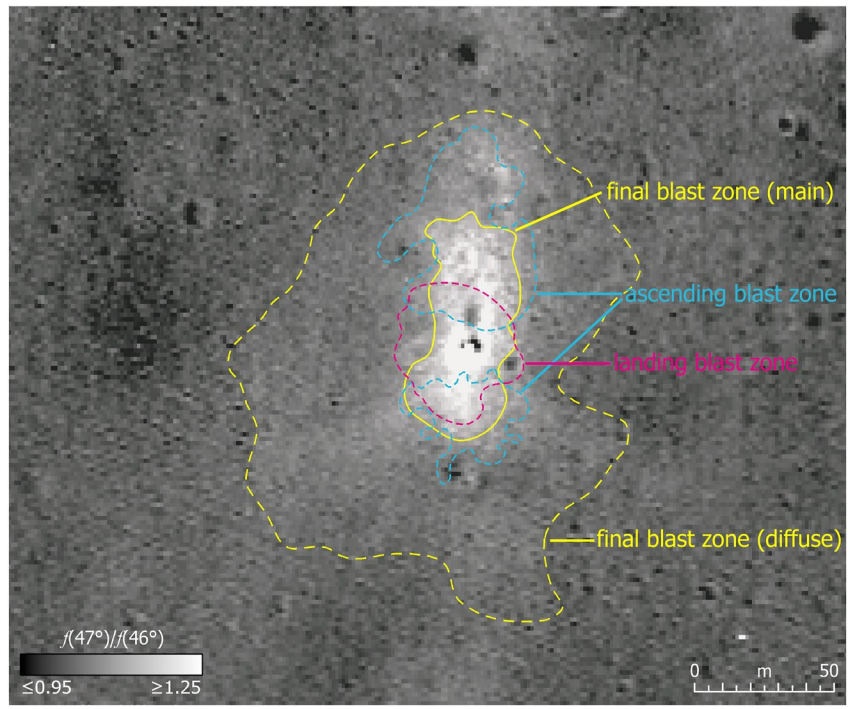


Figure 5. Evolution of the blast zones of Chang'e-5 mission: landing (pink polygon), ascending (turquoise polygons), and final resultant (yellow polygons) blast zones. The background map is the same as Figure 4c in the main text.

value of 1.12 ($1\sigma = 0.05$), very close to that of the landing blast zone (Figure 4a) and apparently higher than the undisturbed background maria, indicating significant changes due to the liftoff activity. Additionally, both blast zones show a trend of decreasing ratio values from the zone centers to the perimeter portions. Due to its larger size, the northern zone is characterized by larger ratio values ranging up to ~1.3, compared to the maximum ratio value of ~1.2 for the southern zone.

In addition, we also evaluated the integrated surface disturbance effects caused by the entire Chang'e-5 mission, including both surface landing and ascending activities, using a temporal ratio image calculated from two NAC images acquired after and before the mission. The two employed NAC frames have similar imaging geometries, especially the phase angle (47.0° vs. 46.3°; Table S1 in Supporting Information S1), thus minimizing the reflectance difference introduced by phase angle variations and facilitating the analyses of surface changes caused by the retrorockets' exhaust plumes. Such an after/before temporal ratio image can also be directly compared with photometric studies of landing sites of other lunar missions, for instance, the Chang'e-3 mission (Clegg-Watkins et al., 2016). In this temporal-ratio image (Figure 4c), mare areas surrounding the Chang'e-5 landing site are characterized by relatively uniform ratio values around 1.0 (average value of 1.0051 ± 0.0191; Table S3 in Supporting Information S1), revealing that they remained largely unchanged during the mission activities.

A spatially extensive area with elevated reflectance (compared with the background maria) is observed to encircle the landing site. The central portion of this bright feature is characterized by apparently larger temporal ratios and apparent outlines (represented by the pink dashed polygon in Figure 4c). This central main blast zone is elongated in the north-south direction and measured ~82 × 38 m in dimension and ~2,300 m^2 in surface area. Its spatial extent is broadly consistent with the integration of the landing and ascent blast zones defined above (Figures 4a and 4b), though with some minor variations (Figure 5). The reflectance of the main blast zone increased by ~20% on average relative to the pre-mission surface (Table S3 in Supporting Information S1), indicating considerable plume impingement effects. The marginal portion of the bright feature has relatively smaller temporal-ratio values and diffuse boundaries (the orange dashed polygon in Figure 4c). This diffuse blast zone extends ~20–70 m from the edge of the central blast zone. It is also elongated in the north-south direction, while more irregular in outline than the central blast zone. It is ~173 × 145 m in dimension and measures ~15,336 m^2 in surface area (excluding the central main blast zone). While the main blast zone is generally centered at the Chang'e-5 landing site, the diffuse blast zone extends further westward

to the interior of the "W-110" crater (Figures 2b and 2c), one of the largest craters in the nearby vicinity of the landing site. This observation is similar to the extension of Apollo 12 blast zones to the adjacent Surveyor crater (Clegg et al., 2014; Kaydash & Shkuratov, 2012), showing that the "W-110" crater could serve as a good recipient of the rocket exhaust gases. In this diffuse blast zone, the average surface reflectance only increased by ~5% after the Chang'e-5 mission activities (Table S3 in Supporting Information S1).

We derive two profiles, one in the west-east direction and the other in the north-south direction, across the landing area from the after/before temporal-ratio image to assess reflectance change trends in the blast zones (Figures 4c–4e). The two profiles confirm the decreasing trend of reflectance with distance from the landing site and the distinct reflectance change patterns between the main and diffuse blast zones. In addition, due to the north-south elongated and irregular outlines of these blast zones, the slope of reflectance changes also varies in different directions. In the marginal diffuse blast zone, the slope of the temporal ratio decrease is ~0.002–0.005 m^{-1} in the west-east direction and ~0.002–0.003 m^{-1} in the north-south direction. The reflectance changes much more sharply with distance in the main blast zone, with a changed slope of ~0.03–0.05 m^{-1} in the west-east direction, and ~0.01–0.02 m^{-1} in the north-direction. The change of reflectance in the diffuse blast zone is relatively subtle in the west direction because the "W-110" crater west of the landing site appears to trap the released gases well.

Finally, in addition to the spatial extent of the lunar surface affected by the mission activities, we investigated how the rocket plume impingements altered the physical properties of the blast zone surface through photometric analysis. Two LROC NAC images, acquired at 45° and 58° phase angles (Table S1 in Supporting Information S1) after the Chang'e-5 mission, were selected to calculate the phase-ratio image across the landing area (Figure 6a). The phase ratio is a direct measurement of the steepness or slope of the phase function, which describes the dependence of surface reflectance on the phase angle and is modulated by the complexity of surface micro-structures, for example, surface regolith particle sizes, micro-topography, and unresolved surface roughness (Kaydash et al., 2012; Shkuratov et al., 1994). Examination of the post-mission phase-ratio image shows that considerable variations occur in the blast zones, which are likely attributed to local topographic and morphological features, such as small impact craters and resolved topographic reliefs. The central main blast zone, especially the surface very close to the Chang'e-5 lander, is characterized by slightly smaller phase-ratio values (~98%) than the background mare region (Table S4 in Supporting Information S1). In addition, the western portion of the diffuse blast zone in the wall of the W-110 crater appears as an apparent negative anomaly in the phase-ratio image. We suggest that such an anomaly could be due to the large-scale topography and the illumination condition difference between the two NAC images. The numerator image (M1374414253L) is illuminated from the southeast, and the denominator image (M1385036262R) is illuminated from the southwest. Therefore, the western wall of the crater is relatively brighter in the numerator image than the eastern wall, while the opposite occurs in the denominator images. As a consequence, the western walls of many resolved craters generally have larger ratio values than the eastern walls. The subtle anomaly observed at the main blast zone should be valid, as the landing area is very flat and therefore free of topographical effects on surface reflectance. A negative phase-ratio anomaly corresponds to the decrease of the phase function slope, indicating smoother surface textures and/or finer surface particle sizes than typical mare regolith materials. This observation is consistent with the lateral removal of lunar regolith fines by the engine jets, which destroys the highly micro-porous structure ("fairy castle") of the uppermost lunar regolith layer, resulting in surface smoothing and brightening (Clegg et al., 2014; Kaydash et al., 2011). As the phase curve of the lunar surface is relatively gentle in this segment of moderate phase angles, the observable photometric anomaly at the Chang'e-5 landing site is testimony to considerable changes in surface properties caused by the gas plumes (Kreslavsky et al., 2000). This interpretation is further confirmed by a scatter plot (Figure 6b) of phase-ratio (45°/58°) and reflectance (58°), which reveals a weak correlation between surface reflectance and phase-ratio values for the entire image, but the main blast zone lies away from the trend of background maria and is characterized by relatively higher surface reflectance and smaller phase-ratio values. The diffuse blast zone generally follows the trend of the background materials in the scatter plot, but it is also close to the main blast zone. This observation indicates that the diffuse blast zone has also been altered by mission activities, though to a relatively subtle degree.

4. Discussion

Analyses of high-resolution multi-temporal imaging data acquired from orbit (Figure 4) and the surface (Figure 3) permit the construction of an informative model for the development and evolution of the rocket plume blast

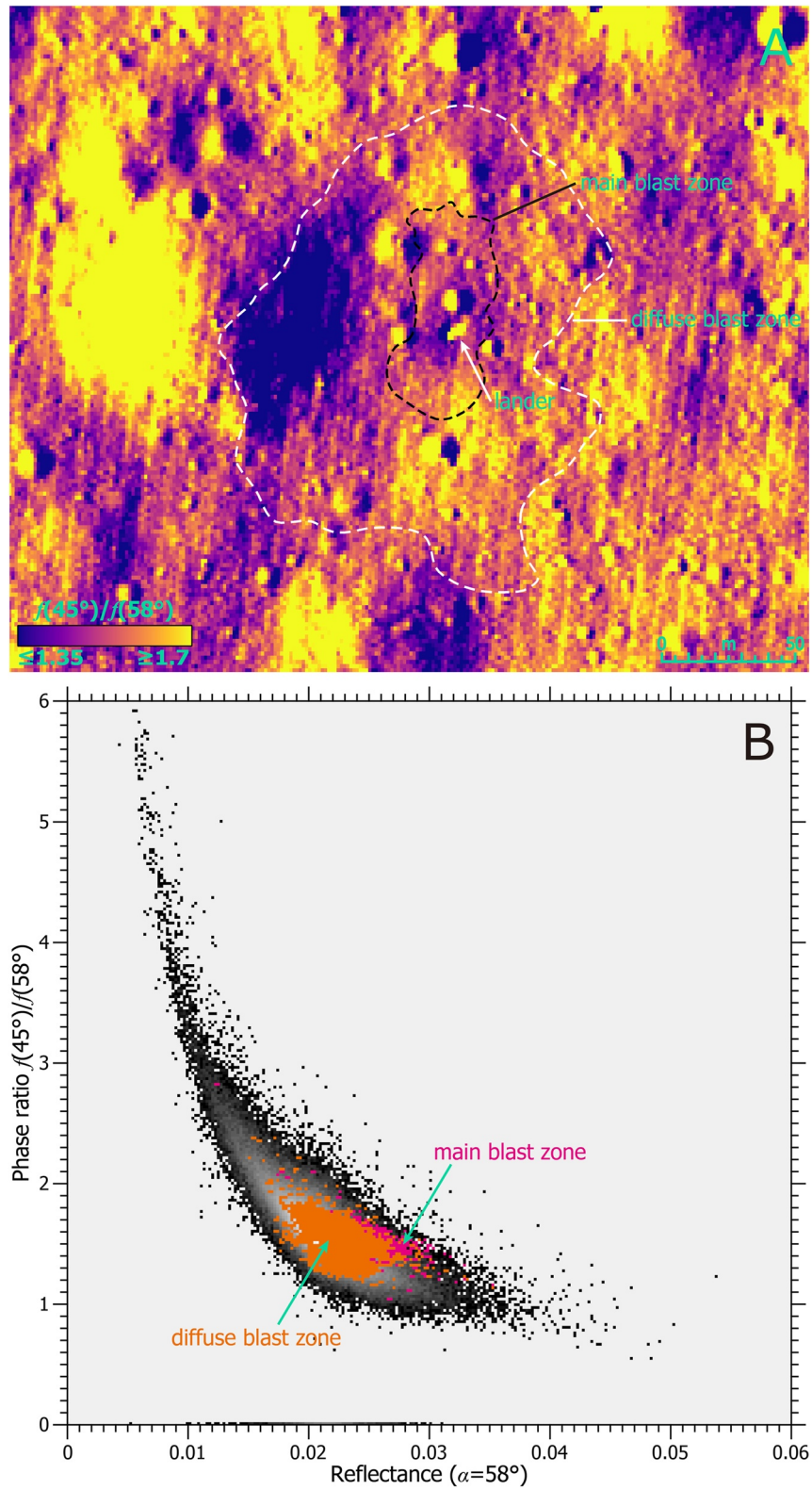


Figure 6. LROC Narrow-Angle Camera (NAC) post-mission phase-ratio image and scatter plot of the Chang'e-5 landing area. (a) Phase-ratio image, $f(45°)/f(58°)$, and (b) scatter plot of phase-ratio $f(45°)/f(58°)$ and reflectance $f(58°)$. The outlines and cloud points of blast zones are pointed out in panels (a and b), respectively. The IDs of source NAC images for phase-ratio calculations are listed in Table S1 of the Supporting Information S1.

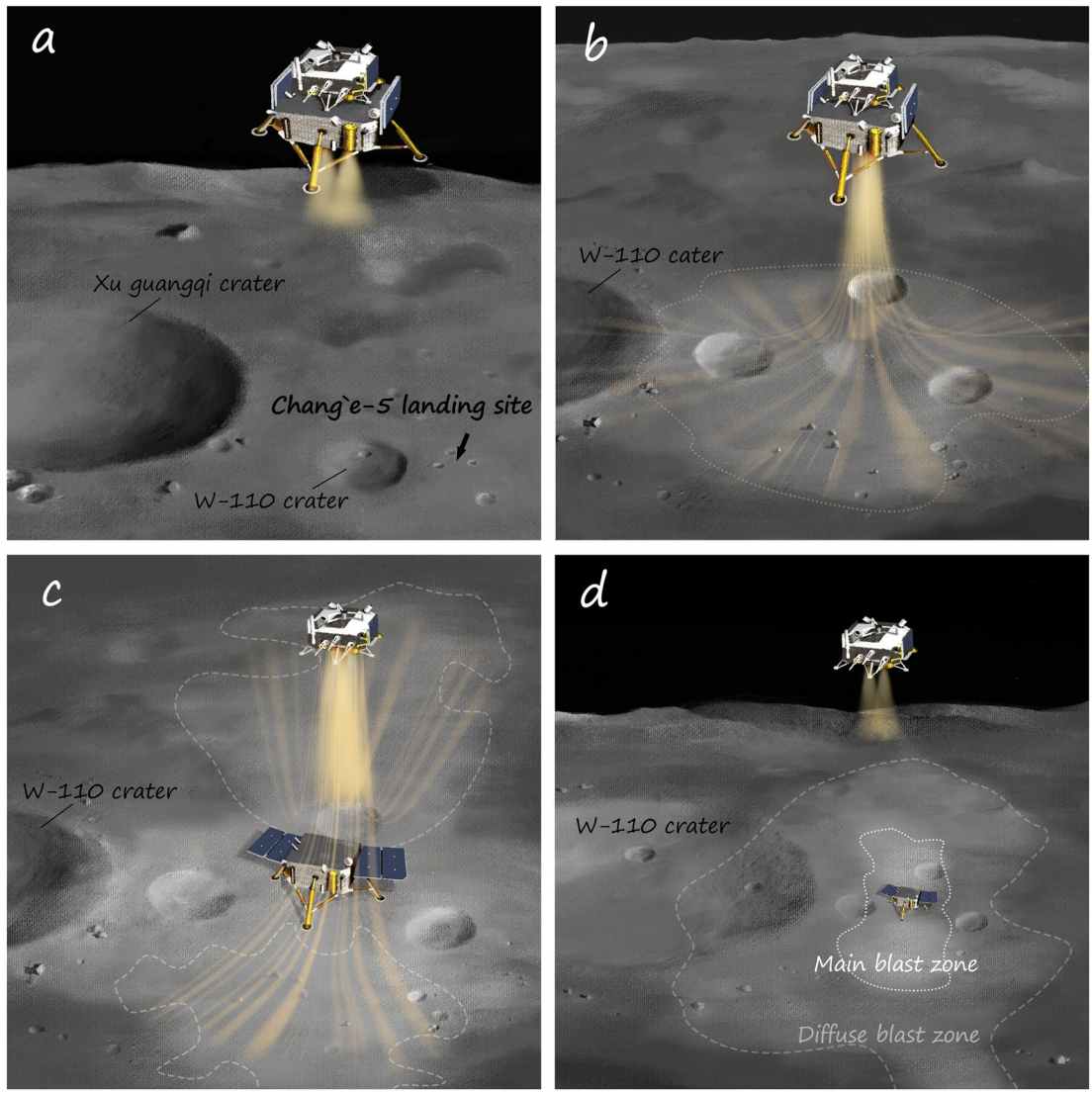


Figure 7. Illustration for the formation and evolution of blast zones introduced by the Chang'e-5 rocket jets. (a) The undisturbed landing area surface before the surface touchdown, (b) the circular blast zone formed by the landing rocket plumes, (c) surface alteration patterns during the surface liftoff, including the largely undisturbed local surface beneath the lander and the two separated blast zones, and (d) the final integrated surface disturbance effects by the Chang'e-5 mission, including the central main blast zone, the diffuse blast zone, and the extension of blast zone into the W-110 crater.

zones produced by the Chang'e-5 landing and ascending procedures (Figures 5 and 7). This, in turn, provides insight into the role of specific mission activities, including spacecraft trajectory and operation maneuvers, in altering the lunar surface.

The initial blast zone, formed by rocket plumes during the powered descending procedure, is approximately circular in outline, with some small marginal lobes (Figure 7b). The circular shape of this landing blast zone is similar to those of the Apollo missions (Clegg et al., 2014; Kaydash & Shkuratov, 2012; Kaydash et al., 2011) but differs from the elongated Chang'e-3 blast zone (Clegg-Watkins et al., 2016). The elongation of the Chang'e-3 blast zone has been interpreted as the result of maneuvering during the hovering and obstacle avoidance stage at a height of ~100 m (Clegg-Watkins et al., 2016). This comparison indicates that relatively fewer maneuvers have been implemented during the Chang'e-5 soft-landing process, consistent with landing trajectory reconstruction results: the Chang'e-3 spacecraft adjusted its position 6 m in the north-south direction and 6 m in the east-west direction (Liu et al., 2014), while the Chang'e-5 re-located only ~4 m in the north-south direction (Yang et al., 2021). The small lobes extending from the edge of the landing blast zone are probably attributed to the accommodating of exhaust gases by small topographical depressions, such as impact craters.

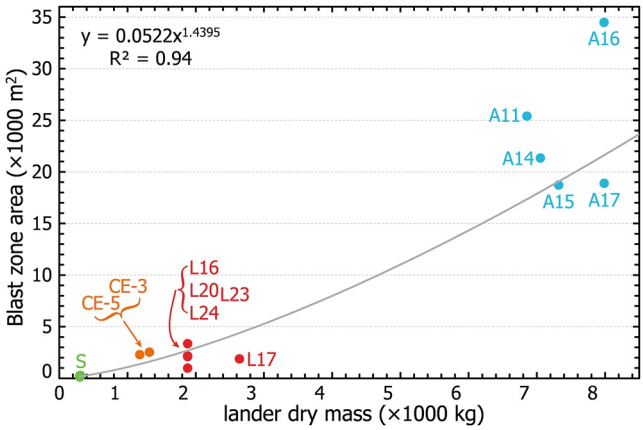


Figure 8. The relationship between lander dry mass and blast zone areas. Plot of blast zone surface area against the lander dry mass for Apollo (A), Luna (L), Surveyor (S), and Chang'e (CE) surface landing missions, and the power law fitting results. The points for all Surveyor missions (1, 5–7) are too close to be distinguished from each other, similar to Luna 20 and 23 points. Chang'e-5 data are from this work and data for other missions are from Clegg-Watkins et al. (2016).

Additional blast zones are observed to be formed by the impingement of ascent engine jets during the surface liftoff procedure. Interestingly, the ascent blast zone consists of two small, separated sub-zones, while the lunar surface in the near vicinity of the Chang'e-5 lander appears to be free of exhaust plume effects (Figure 7c). We interpret the unusual spatial distribution of the blast zone as the result of the obstruction of the lander platform to the engine jet plumes during the surface liftoff and the related special design for plume deflection (Shu et al., 2021). The apparently larger size of the north sub-zone (~2.7 times the surface area of the south one) is likely to be an indicator of the north-trending flight trajectory in the initial stage of the surface liftoff. Previous lunar surface liftoff activities, like those during the Apollo and Luna missions, might also have produced similar ascent blast zones. However, due to the absence of high-resolution landing area images acquired between the landing and surface liftoff, prior landing area analyses were only able to identify the final blast zone formed by both landing and ascent engine jets, rather than independently separating the ascent blast zones (Clegg et al., 2014; Clegg-Watkins et al., 2016; Kaydash et al., 2011). Lunar surface disturbances by the ascent engine plumes were previously assumed to be negligible because the usage of the lander as the launch pad would disrupt the exhaust gas flows and thus protect the lunar surface beneath the lander (Clegg et al., 2014). Our investigation clearly shows that the very local surface beneath the lander has indeed been protected by the launch pad, but the adjacent surface was significantly disturbed by liftoff activities. The surface area altered by the Chang'e-5 ascent activity is nearly two times larger than the area affected during the landing phase (cf. Figures 4a and 4b), indicating that the plume impingement effects of the surface liftoff are probably comparable with or even more significant than that of the lunar landing. We propose the following as a plausible interpretation: though the main landing engine is over two times more powerful than the main ascent engine (7,500 vs. 3,000 N maximum thrust), the landing engine might only operate at a lower power when the lander approached the lunar surface (Zhang et al., 2022), while the ascent engine should have operated at its full capacity to lift and accelerate the ascent stage rapidly, thus having a much more significant effect on the disturbance and removal of lunar surface materials.

Our characterization of lunar surface disturbance effects by rocket engine plumes provides an instructive framework for future lunar exploration activities. This is particularly important in light of the current trend, in which dozens of spacecraft are planned to land on the Moon in the coming years and permanent lunar outposts are in formulation; the latter may involve multiple landing and ascent activities at the same lunar site. Data from the Apollo missions showed that clouds of lunar regolith and dust with particle density up to 10^{13} m^{-3} were lifted during the landing phase (Immer, Lane et al., 2011). Small particles were accelerated sufficiently by the plume flows up to ~2 km/s, which, if encountered, would heavily impact and damage lunar surface materials and instrument packages emplaced on the lunar surface (Brownlee et al., 1972). In the case of astronautical activities similar to Chang'e-5, to protect the humans and assets on the lunar surface, a safe distance from the landing/launch pad should be at least 200 m away. This minimum safe distance is greater than the maximum traverses from the landing module in the Apollo 11 mission (~60 m) and comparable with that for the Apollo 12 mission (~440 m), the only two Apollo surface missions that did not use any wheeled vehicles. This comparison shows that wheeled vehicles, either hand-pulled ones (such as that used in Apollo 14) or advanced roving ones (such as those used in Apollo 15–17), are essential to transport tools and instruments efficiently on the lunar surface during the construction of permanent lunar outposts.

In addition, lunar surface missions in the coming years are likely to use much heavier vehicles, for instance, the SpaceX's Starship that has been selected by NASA as the Human Landing System to transfer astronauts to the surface of the Moon beginning in 2025. The Starship lander is designed with the capacity of carrying over 100 tons of cargo to the lunar surface (SpaceX, 2020). Based on the lander dry mass and blast zones of Chang'e-5 (this study) and previous landed missions (Clegg-Watkins et al., 2016), we confirm that the main blast zone area is well related to the lander dry mass and the relationship can be fitted with a power law function ($R^2 = 0.94$; Figure 8 and Lorenz, 2016, better than a quadratic polynomial fitting ($R^2 = 0.9077$; Figure S1 in Supporting Information S1

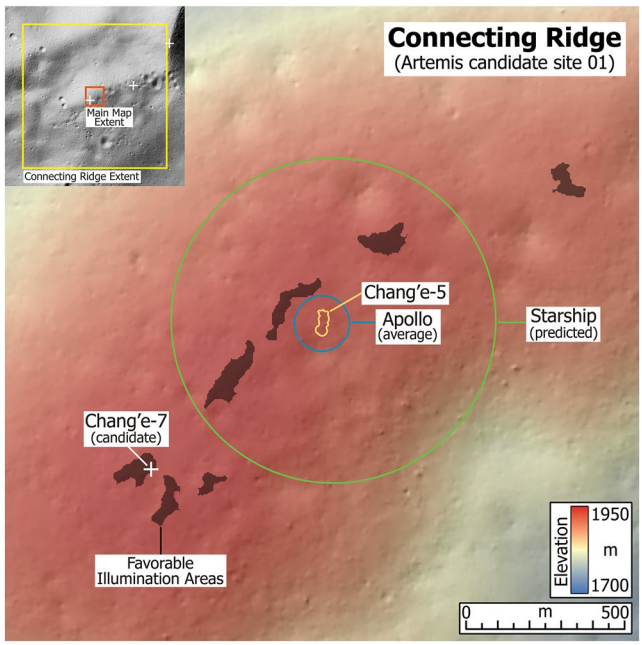


Figure 9. Comparison of the main blast zone areas of Chang'e-5, Apollo (average) and SpaceX Starship (predicted). The background image is a LOLA shaded relief map (Barker et al., 2021) of the central 2 × 2 km portion of the Shackleton-de Gerlache Connecting Ridge, one of the candidate landing regions of NASA's Artemis III mission (https://www.nasa.gov/press-release/nasa-identifies-candidate-regions-for-landing-next-americans-on-moon). The full extent of the Connecting Ridge regions is outlined by the yellow square in the upper left insert map. The dark gray areas are regions larger than 2,500 m^2 with an average solar illumination of over 70% between 1 January 2024 and 1 January 2026 (Barker et al., 2021) and the white crosses (in both the main and insert maps) are the candidate landing sites for China's Chang'e-7 lunar polar mission (Zhang et al., 2020).

and Clegg-Watkins et al., 2016)). Such a relationship would project a central main blast zone with a surface area at the scale of square kilometers for the Starship lunar lander, over one order of magnitude more extensive than any previous lunar surface mission (Figure 9). The marginal diffuse blast zone would be even larger, probably nearly 10 times the size of the central main blast zone. In addition, the landing of the Starship Human Landing System in the lunar south polar region would also contaminate lunar surface materials over an extensive area, including volatile materials in many cold traps. These volatiles hold great promise for both solar system history studies and extra-terrestrial resource utilization and are being targeted by multiple planned lunar polar missions, such as China's Chang'e-7 (Figure 9). We conclude that the mitigation of impingement effects by rocket exhaust plumes needs to be seriously considered and assessed in the design of forthcoming lunar landed missions and permanent lunar bases, such as the International Lunar Research Station and the Artemis Base Camp.

5. Conclusions

We assess the surface disturbance at the Chang'e-5 mission landing site through photometric analysis of high-resolution multi-temporal Chang'e-5 surface images and LRO orbital images. About 1.9 and 0.4 tons of propellant were consumed during the powered landing and ascend procedures, respectively. The basaltic mare plain at the landing site is superposed by many sub-kilometer impact craters, which appear to efficiently contain the released engine jets. The sequences of Chang'e-5 landing images reveal a four-stage evolution for the interactions between landing rocket exhaust gases and lunar surface materials, involving many significant phenomena, such as dust devil and sheet, radial dust streak, and displacements of cobbles and regolith particles. Temporal-ratio calculations of LROC NAC images demonstrate apparent surface changes introduced by the Chang'e-5 landing and ascent plumes. The landing blast zone is nearly circular (~1,600 m^2) and the ascent blast zone consists of two separated sub-areas (3,400 km^2 in total). This is the first direct evaluation of plume impingement effects during lunar liftoff, which are unexpectedly much more extensive and significant than previously assumed and probably surpass those during a lunar landing. The final disturbed lunar surface is characterized by a central main blast zone (~2,300 m^2) surrounded by a marginal diffuse blast zone (~15,300 m^2). Phase-ratio image analyses suggest that the plume impingement destroys the micro-porous structure of the uppermost regolith layer at the landing site, resulting in surface smoothing and brightening. The power law relationship between blast zone size and lander dry mass derived from Chang'e-5 and previous lunar landing missions predicts that future heavy lunar landers, such as SpaceX's Starship Human Landing System, may disturb the lunar surface over square kilometers. Our results provide a unique insight from Chang'e-5 mission activities, and an informative frame of reference for the planning of future lunar exploration, including the design and construction of lunar surface experiment packages and permanent lunar bases.

Data Availability Statement

The Chang'e-5 surface image data are archived at the Lunar and Planetary Data Release System (LCAM: http://www.dx.doi.org/10.12350/CLPDS.GRAS.CE5.LCAM-2A.vA; PCAM: http://www.dx.doi.org/10.12350/CLPDS.GRAS.CE5.PCAM-2B.vA), the LRO LROC NAC image data can be found at Robinson (2009a), the LROC NAC DTM topography data are available from Robinson (2009b), the Kaguya TC image data are archived at SELENE Data Archive (https://darts.isas.jaxa.jp/planet/pdap/selene/), and the SLDEM2015 topography data are archived at the PDS Geosciences Node (https://pds-geosciences.wustl.edu/lro/lro-l-lola-3-rdr-v1/lrolol_1xxx/data/sldem2015/). The data used to plot Figure 8 are accessible at Zenodo (Qiao, 2023).

Acknowledgments
We acknowledge the Ground Research and Application System (GRAS) of China's Lunar and Planetary Exploration Program for providing the Chang'e-5 scientific data, and the LRO and Kaguya mission teams for providing the orbital data sets. This work was supported jointly by National Key Research and Development Program of China (2022YFF0503100), CNSA pre-research project on Civil Aerospace Technologies (D020204), National Natural Science Foundation of China (42241107, 11941001, 41972322, 12273044, 42201424), Young Scholars Program of Shandong University, Weihai (202207), State Key Laboratory of Lunar and Planetary Sciences of M.U.S.T (Macau FDCT Grant SKL-LPS(MUST)-2021-2023), the Key Research Program of the Chinese Academy of Sciences (KGFZD-145-2023-15), and the Science and Technology Development Fund, Macau SAR (0049/2020/A1).

References

Anderson, J. A., Sides, S. C., Soltesz, D. L., Sucharski, T. L., & Becker, K. J. (2004). Modernization of the integrated software for imagers and spectrometers. In *35th lunar and planetary science conference*. Lunar and Planetary Institute. abstract #2039.

Barker, M. K., Mazarico, E., Neumann, G. A., Smith, D. E., Zuber, M. T., & Head, J. W. (2021). Improved LOLA elevation maps for south pole landing sites: Error estimates and their impact on illumination conditions. *Planetary and Space Science*, *203*, 105119. https://doi.org/10.1016/j.pss.2020.105119

Barker, M. K., Mazarico, E., Neumann, G. A., Zuber, M. T., Haruyama, J., & Smith, D. E. (2016). A new lunar digital elevation model from the Lunar Orbiter Laser Altimeter and SELENE Terrain Camera. *Icarus*, *273*, 346–355. https://doi.org/10.1016/j.icarus.2015.07.039

Brownlee, D. E., Bucher, W., & Hodge, P. (1972). Primary and secondary micrometeoroid impact rate on the lunar surface: A direct measurement. In *Analysis of surveyor 3 material and photographs returned by Apollo 12* (pp. 143–151). National Aeronautics and Space Administration.

Clegg, R. N., Jolliff, B. L., Robinson, M. S., Hapke, B. W., & Plescia, J. B. (2014). Effects of rocket exhaust on lunar soil reflectance properties. *Icarus*, *227*, 176–194. https://doi.org/10.1016/j.icarus.2013.09.013

Clegg-Watkins, R. N., Jolliff, B. L., Boyd, A., Robinson, M. S., Wagner, R., Stopar, J. D., et al. (2016). Photometric characterization of the Chang'e-3 landing site using LROC NAC images. *Icarus*, *273*, 84–95. https://doi.org/10.1016/j.icarus.2015.12.010

CNSA (China National Space Administration) and Roscosmos. (2021). International lunar research station (ILRS) guide for partnership (V1.0). Retrieved from http://www.cnsa.gov.cn/english/n6465652/n6465653/c6812150/content.html

Gold, T. (1970). Apollo 11 and 12 close-up photography. *Icarus*, *12*(3), 360–375. https://doi.org/10.1016/0019-1035(70)90005-9

Gou, S., Yue, Z., Di, K., Wan, W., Liu, Z., Liu, B., et al. (2020). In situ spectral measurements of space weathering by Chang'e-4 rover. *Earth and Planetary Science Letters*, *535*, 116117. https://doi.org/10.1016/j.epsl.2020.116117

Hapke, B. W. (1972). The lunar disturbance effect. *The Moon*, *3*(4), 456–460. https://doi.org/10.1007/BF00562465

Haruyama, J., Hara, S., Hioki, K., Iwasaki, A., Morota, T., Ohtake, M., et al. (2012). Lunar global digital terrain model dataset produced from SELENE (Kaguya) terrain camera stereo observations. In *43rd lunar and planetary science conference*. Lunar and Planetary Institute. abstract #1200.

Haruyama, J., Matsunaga, T., Ohtake, M., Morota, T., Honda, C., Yokota, Y., et al. (2008). Global lunar-surface mapping experiment using the Lunar Imager/Spectrometer on SELENE. *Earth Planets and Space*, *60*(4), 243–255. https://doi.org/10.1186/BF03352788

Head, J. W., & Wilson, L. (2017). Generation, ascent and eruption of magma on the Moon: New insights into source depths, magma supply, intrusions and effusive/explosive eruptions (Part 2: Predicted emplacement processes and observations). *Icarus*, *283*, 176–223. https://doi.org/10.1016/j.icarus.2016.05.031

Henriksen, M. R., Manheim, M. R., Burns, K. N., Seymour, P., Speyerer, E. J., Deran, A., et al. (2017). Extracting accurate and precise topography from LROC narrow angle camera stereo observations. *Icarus*, *283*, 122–137. https://doi.org/10.1016/j.icarus.2016.05.012

Hiesinger, H., Head, J. W., Wolf, U., Jaumann, R., & Neukum, G. (2011). Ages and stratigraphy of lunar mare basalts: A synthesis. *Geological Society of America Special Paper*, *477*, 1–51. https://doi.org/10.1130/2011.2477(01)

Hong, X., Guo, S., Han, Q., & Pan, Z. (2022). Development and flight performance of Chang'e-5 probe propulsion system. *Journal of Propulsion Technology*, *43*, 6–19. https://doi.org/10.13675/j.cnki.tjjs.210853

Hurwitz, D. M., Head, J. W., & Hiesinger, H. (2013). Lunar sinuous rilles: Distribution, characteristics, and implications for their origin. *Planetary and Space Science*, *79–80*, 1–38. https://doi.org/10.1016/j.pss.2012.10.019

Immer, C., Lane, J., Metzger, P., & Clements, S. (2011). Apollo video photogrammetry estimation of plume impingement effects. *Icarus*, *214*(1), 46–52. https://doi.org/10.1016/j.icarus.2011.04.018

Immer, C., Metzger, P., Hintze, P. E., Nick, A., & Horan, R. (2011). Apollo 12 lunar module exhaust plume impingement on lunar surveyor III. *Icarus*, *211*(2), 1089–1102. https://doi.org/10.1016/j.icarus.2010.11.013

Kaydash, V., Shkuratov, Y., Korokhin, V., Velichko, S., & Videen, G. (2018). The lunar surface around extremely fresh craters. *Icarus*, *311*, 258–270. https://doi.org/10.1016/j.icarus.2018.04.024

Kaydash, V., Shkuratov, Y., Korokhin, V., & Videen, G. (2011). Photometric anomalies in the Apollo landing sites as seen from the lunar reconnaissance orbiter. *Icarus*, *211*(1), 89–96. https://doi.org/10.1016/j.icarus.2010.08.024

Kaydash, V., Shkuratov, Y., & Videen, G. (2012). Phase-ratio imagery as a planetary remote-sensing tool. *Journal of Quantitative Spectroscopy and Radiative Transfer*, *113*(18), 2601–2607. https://doi.org/10.1016/j.jqsrt.2012.03.020

Kaydash, V. G., & Shkuratov, Y. G. (2012). Structural disturbances of the lunar surface caused by spacecraft. *Solar System Research*, *46*(2), 108–118. https://doi.org/10.1134/S0038094612020050

Kreslavsky, M. A., Shkuratov, Y. G., Velikodsky, Y. I., Kaydash, V. G., Stankevich, D. G., & Pieters, C. M. (2000). Photometric properties of the lunar surface derived from Clementine observations. *Journal of Geophysical Research*, *105*(E8), 20281–20295. https://doi.org/10.1029/1999JE001150

Li, C., Hu, H., Yang, M.-F., Pei, Z.-Y., Zhou, Q., Ren, X., et al. (2022). Characteristics of the lunar samples returned by the Chang'E-5 mission. *National Science Review*, *9*(2), nwab188. https://doi.org/10.1093/nsr/nwab188

Liu, J.-J., Yan, W., Li, C.-L., Tan, X., Ren, X., & Mu, L.-L. (2014). Reconstructing the landing trajectory of the CE-3 lunar probe by using images from the landing camera. *Research in Astronomy and Astrophysics*, *14*(12), 1530–1542. https://doi.org/10.1088/1674-4527/14/12/003

Lorenz, R. D. (2016). Lander rocket exhaust effects on Europa regolith nitrogen assays. *Planetary and Space Science*, *127*, 91–94. https://doi.org/10.1016/j.pss.2016.04.008

Melosh, H. J. (1989). *Impact cratering: A geologic process*. Oxford University Press.

Metzger, P. T., Smith, J., & Lane, J. E. (2011). Phenomenology of soil erosion due to rocket exhaust on the Moon and the Mauna Kea lunar test site. *Journal of Geophysical Research*, *116*(E6), E06005. https://doi.org/10.1029/2010JE003745

NASA. (2020). NASA's plan for sustained lunar exploration and development. Retrieved from https://www.nasa.gov/feature/nasa-outlines-lunar-surface-sustainability-concept

NASA Manned Space Center. (1972). Apollo 16 technical debrief. Retrieved from https://www.hq.nasa.gov/alsj/a16/a16tecdbrf.html

NASA Manned Space Center. (1969). Apollo 11 technical crew debriefing. Retrieved from https://www.hq.nasa.gov/alsj/a11/a11tecdbrf.html

Pickrell, J. (2022). These six countries are about to go to the Moon—Here's why. *Nature*, *605*(7909), 208–211. https://doi.org/10.1038/d41586-022-01252-7

Prem, P., Hurley, D. M., Goldstein, D. B., & Varghese, P. L. (2020). The evolution of a spacecraft-generated lunar exosphere. *Journal of Geophysical Research: Planets*, *125*(8), e2020JE006464. https://doi.org/10.1029/2020JE006464

Qian, Y., Xiao, L., Head, J. W., & Wilson, L. (2021b). The long sinuous rille system in northern Oceanus Procellarum and its relation to the Chang'e-5 returned samples. *Geophysical Research Letters*, *48*(11), e2021GL092663. https://doi.org/10.1029/2021GL092663

Qian, Y., Xiao, L., Head, J. W., van der Bogert, C. H., Hiesinger, H., & Wilson, L. (2021). Young lunar mare basalts in the Chang'e-5 sample return region, northern Oceanus Procellarum. *Earth and Planetary Science Letters*, *555*, 116702. https://doi.org/10.1016/j.epsl.2020.116702

Qian, Y., Xiao, L., Wang, Q., Head, J. W., Yang, R., Kang, Y., et al. (2021). China's Chang'e-5 landing site: Geology, stratigraphy, and provenance of materials. *Earth and Planetary Science Letters*, *561*, 116855. https://doi.org/10.1016/j.epsl.2021.116855

Qiao, L. (2023). Lunar landing mission: Lander mass & blast zone area [Dataset]. Zenodo. https://doi.org/10.5281/zenodo.7811841

Qiao, L., Chen, J., Xu, L., Wan, S., Cao, H., Li, B., & Ling, Z. (2021). Geology of the Chang'e-5 landing site: Constraints on the sources of samples returned from a young nearside mare. *Icarus*, *364*, 114480. https://doi.org/10.1016/j.icarus.2021.114480

Qiao, L., Xu, L., Yang, Y., Xie, M., Chen, J., Fang, K., & Ling, Z. (2021). Cratering records in the Chang'e-5 mare unit: Filling the "age gap" of the lunar crater chronology and preparation for its recalibration. *Geophysical Research Letters*, *48*(22), e2021GL095132. https://doi.org/10.1029/2021GL095132

Roberts, L. (1963). The action of a hypersonic jet on a dust layer. In *Institute of the aerospace sciences 31st annual meeting* (pp. 63–50). Institute of the Aerospace Sciences.

Robinson, M. (2009a). LRO MOON LROC 2 EDR V1.0 [Dataset]. NASA Planetary Data System (PDS). https://doi.org/10.17189/1520250

Robinson, M. (2009b). LRO MOON LROC 5 RDR V1.0 [Dataset]. NASA Planetary Data System (PDS). https://doi.org/10.17189/1520341

Robinson, M. S., Boyd, A. K., Denevi, B. W., Lawrence, S. J., McEwen, A. S., Moser, D. E., et al. (2015). New crater on the Moon and a swarm of secondaries. *Icarus*, *252*, 229–235. https://doi.org/10.1016/j.icarus.2015.01.019

Robinson, M. S., Brylow, S. M., Tschimmel, M., Humm, D., Lawrence, S. J., Thomas, P. C., et al. (2010). Lunar reconnaissance orbiter camera (LROC) instrument overview. *Space Science Reviews*, *150*(1), 81–124. https://doi.org/10.1007/s11214-010-9634-2

Shkuratov, Y. G., Starukhina, L. V., Kreslavsky, M. A., Opanasenko, N. V., Stankevich, D. G., & Shevchenko, V. G. (1994). Principle of undulatory invariance in photometry of atmosphereless celestial bodies. *Icarus*, *109*(1), 168–190. https://doi.org/10.1006/icar.1994.1084

Shu, Y., Xing, Z., Zhang, X., Zhang, W., Zhang, Z., Ye, Q., et al. (2021). Designing and implementing the liftoff of Chang'e-5 spacecraft from the Moon. *Scientia Sinica Technologica*, *51*(12). https://doi.org/10.1360/sst-2021-0122

Smith, D. E., Zuber, M. T., Jackson, G. B., Cavanaugh, J. F., Neumann, G. A., Riris, H., et al. (2010). The lunar orbiter laser altimeter investigation on the lunar reconnaissance orbiter mission. *Space Science Reviews*, *150*(1), 209–241. https://doi.org/10.1007/s11214-009-9512-y

SpaceX (Space Exploration Technologies Corp.). (2020). Starship users guide: Revision 1.0. Retrieved from https://www.spacex.com/media/starship_users_guide_v1.pdf

Speyerer, E. J., Povilaitis, R. Z., Robinson, M. S., Thomas, P. C., & Wagner, R. V. (2016). Quantifying crater production and regolith overturn on the Moon with temporal imaging. *Nature*, *538*(7624), 215–218. https://doi.org/10.1038/nature19829

Watkins, R. N., Metzger, P. T., Eppler, D., Munk, M., Dove, A., Jolliff, B. L., & Moriarty, D. P. (2020). Understanding rocket exhaust effects in polar regions during powered descent on the Moon. In *Artemis III science definition team white papers*. Lunar and Planetary Institute.

Xu, L., & Qiao, L. (2022). Formation age of the Rima Sharp sinuous rill on the Moon, source of the returned Chang'e-5 samples. *Astronomy & Astrophysics*, *657*, A42. https://doi.org/10.1051/0004-6361/202142092

Yang, P., Huang, Y., Li, P., Liu, S., Shan, Q., & Zheng, W. (2021). Trajectory determination of Chang'E-5 during landing and ascending. *Remote Sensing*, *13*(23), 4837. https://doi.org/10.3390/rs13234837

Zhang, H., Du, Y., Li, F., Zhang, H., Ma, J., Sheng, L., & Wu, K. (2020). Proposals for sites selection of soft landing on lunar south polar region. *Journal of Deep Space Exploration*, *7*(3), 232–240. https://doi.org/10.15982/j.issn.2095-7777.2020.20191003002

Zhang, H., Li, C., You, J., Zhang, X., Wang, Y., Chen, L., et al. (2022). The investigation of plume-regolith interaction and dust dispersal during Chang'E-5 descent stage. *Aerospace*, *9*(7), 358. https://doi.org/10.3390/aerospace9070358

Zhou, C., Jia, Y., Liu, J., Li, H., Fan, Y., Zhang, Z., et al. (2022). Scientific objectives and payloads of the lunar sample return mission—Chang'E-5. *Advances in Space Research*, *69*(1), 823–836. https://doi.org/10.1016/j.asr.2021.09.001

Erratum

The originally published version of this article contained typographical error. In the sixth sentence of the Abstract, the area unit should read "~3,400 m^2". The error has been corrected, and this version may be considered the authoritative version of record.